Available online at www.sciencedirect.com

ScienceDirect

Ceramics International 39 (2013) 9619–9626

CERAMICS INTERNATIONAL

www.elsevier.com/locate/ceramint

Structural characterisation and Li conductivity of $Li_{1/2-x}Sr_{2x}La_{1/2-x}TiO_3$ $(0<x<0.5)$ perovskites

M.E. Sotomayor[a], A. Várez[a,*], W. Bucheli[b], R. Jimenez[b], J. Sanz[b]

[a]Departamento de Ciencia e Ingeniería de Materiales, IAAB, Universidad Carlos III de Madrid, Avda. Universidad 30, 28911-Leganés, Spain
[b]Instituto de Ciencia de Materiales de Madrid, CSIC, 28049 Cantoblanco, Spain

Received 25 March 2013; received in revised form 18 May 2013; accepted 20 May 2013
Available online 30 May 2013

Abstract

The crystal structure and electric properties of different compositions of the $Li_{1/2}La_{1/2}TiO_3$–$SrTiO_3$ system, which were prepared by solid-state reaction, were investigated. The limits of the $Li_{1/2-x}Sr_{2x}La_{1/2-x}TiO_3$ solid solution ($0.0625 \leq x \leq 0.25$) were established by X-ray diffraction (XRD) and scanning electron microscopy (SEM) analyses. All compositions exhibited a single cubic perovskite structure ($a_c \approx 3.87$–3.90 Å; SG Pm-3m), as determined by XRD analysis. Along the solid solution, a positive deviation from Vegard's law was observed. This deviation was related to the occurrence of incipient La and Sr segregation/clustering in apparently homogeneous single phases. The room-temperature Li conductivity ranged from 7.4×10^{-4} to 2.8×10^{-5} S cm^{-1}, and the activation energy of the samples was close to 0.33 eV, similar to that of the best Li-ion conductors. The substitution of Li by Sr decreased the number of effective vacancies ($n_t = [Li] + \Upsilon$, where Υ is the nominal A-vacancy concentration), which appreciably reduced the Li conductivity when the n_t approached the 3D percolation threshold. In this series, the percolation threshold is greater than expected, which reinforces the idea that the incipient segregation is responsible for the deviation from Vegard's law.

Keywords: Lithium conductivity; Perovskite structure; XRD characterisation

1. Introduction

Over the last two decades, the search for new materials with high lithium ionic conductivity has attracted considerable interest. A wide variety of solid electrolytes with high ionic conductivities and potential applications in all-solid high-energy batteries and other electrochemical devices have been reported.

Since the discovery of the fast ion conductor $Li_{0.5}La_{0.5}TiO_3$ (LLTO) by Belous et al. [1] and Inaguma et al. [2], researchers have extensively sought to understand its high lithium conductivity. In this sense, several chemical substitutions have been performed on this material. Most of them have been mentioned in the review by Stramare et al. [3], who focused on the ionic conductivity–composition–structure relationship of LLTO and related materials.

The substitutions of Ti (located at the B sites of perovskites) by trivalent cations such as Al result in an increase in the conductivity [4], whereas substitutions by tetravalent cations, such as Zr, Sn, Mn or Ge [5] diminish it. The replacement of Ti by pentavalent cations such as Nb [6,7] or Ta [8] decreases the ionic conductivity despite the increase in the A-site vacancy concentration. The substitution of La^{3+} by other trivalent rare-earth (RE) metals in these perovskites produced a single phase with the formula $RE_{2/3-x}Li_{3x}TiO_3$ but did not improve the ionic conductivity of this series (10^{-3} S cm^{-1} at room temperature) [9–11]. The partial substitutions of La by larger cations, such as Sr, Ba or Na, produce variable effects [12]. In the case of Sr, the ionic conductivity slightly increases at low degrees of substitution (5 %mol). In Ba-containing samples, no single phases are obtained, whereas, in Na-containing samples, the conductivity decreases rapidly with cation dilution [12].

Recently, the $Li_xSr_xLa_{2/3-x}TiO_3$ series has been revisited [13]. In these samples, La^{3+} cations were substituted by (Sr^{2+}+Li^+) (line 3 of the ternary phase diagram in Fig. 1), and the number

---

*Corresponding author. Tel.: +34 91 6249484; fax: +34 91 6249430.
E-mail address: alvar@ing.uc3m.es (A. Várez).

0272-8842/$ - see front matter
http://dx.doi.org/10.1016/j.ceramint.2013.05.083

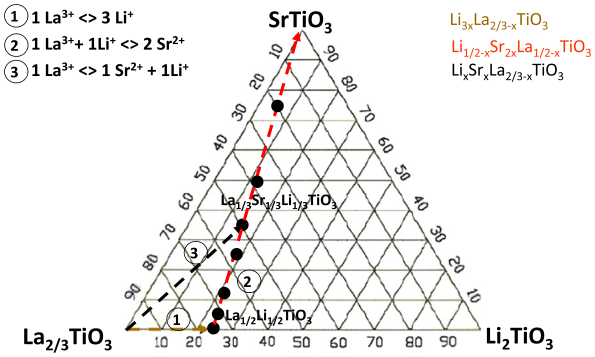

Fig. 1. $La_{2/3}TiO_3$–$SrTiO_3$–Li_2TiO_3 compositional diagram illustrating the Sr-doping of LLTO perovskites. The solid solutions investigated in this paper are indicated with bold circles along arrow number 2. Other substitution schemes previously studied are also included ($Li_{3x}La_{2/3-x}TiO_3$ along line number 1 and $Li_xSr_xLa_{2/3-x}TiO_3$ along line number 3).

of nominal A vacancies decreased along the series. However, the effective number of vacancies, which is calculated according to the expression $n_t = [\mathrm{Li}] + \Upsilon$ [14] (Υ = nominal A-site vacancy concentration), remained constant.

In the present work, we have prepared different compositions of the $La_{1/2}Li_{1/2}TiO_3$–$SrTiO_3$ join (line 2) of the ternary phase diagram. In this case, (La^{3+}+Li^{+}) have been replaced by two Sr^{2+} cations, thereby maintaining the charge balance and the amount of nominal vacancies. The limits of the solid solution have been investigated by a combination of XRD and SEM techniques. Structural features were deduced from the Rietveld analysis of XRD patterns, and the Li mobility was investigated by impedance spectroscopy (IS). The dependence of the conductivity on the effective vacancy concentration is also discussed.

2. Experimental

2.1. Sample preparation

Reagent-grade Li_2CO_3, La_2O_3, $SrCO_3$ and TiO_2 were measured according to the formula $Li_{1/2-x}Sr_{2x}La_{1/2-x}TiO_3$ for $x = 0.0312$, 0.0625, 0.125, 0.15, 0.25, 0.3125 and 0.375. High-purity reagents were purchased from Aldrich. Before being weighed, the La_2O_3 was heated at 800 °C for 4 h for decarbonation. These reagents were ground together in an agate mortar and heated at 800 °C for 12 h. The reground products were cold-pressed at 150 MPa and heated at 1150 °C for 12 h. Finally, powders were uniaxially pressed and heated at 1300 °C for 6 h. To avoid lithium losses, the heating rate used in the thermal treatments was 1 °C/min [15,16]. The cooling rate of the last treatment was 5 °C/min.

2.2. Sample characterisation

X-ray diffraction powder (XRD) patterns were recorded on a Philips X'Pert diffractometer equipped with a CuKα radiation source. This instrument has a ($\theta/2\theta$) Bragg–Brentano geometry and is equipped with a curved graphite monochromator. Data were taken with a 0.5° divergence slit, a receiving slit of 0.01° and a set of soller slits with 1° of axial divergence. The 2θ range analysed was 5–120° with a step scan of 0.02° and a counting time of 8 s per step. XRD patterns were indexed and analysed by the Rietveld method using the Fullprof programme [17].

The microstructure of sintered samples was analysed with a Philips XL30 scanning electron microscope equipped with a backscattered-electron detector (BSE) and an energy-dispersive analyser (EDAX 4i). Elemental analyses were performed with a fixed take-off angle, live time (60 s) and acceleration voltage (15 kV). For each detected phase, at least five analyses were performed on different crystallites. Due to the insulator character of the samples, sintered samples were coated with a very thin layer of carbon.

Electrical measurements were performed by impedance spectroscopy on pellets with a diameter of 12 mm and a thickness of 1 mm. These samples were prepared by being uniaxially pressed and sintered at 1300 °C for 6 h. The relative densities of the samples with $0 < x \leq 0.25$ were approximately 90%, whereas samples with high Sr contents exhibited lower densities. The electrical measurements were performed on a parallel-plate capacitor configuration. Gold electrodes (Dupont QG150 Au paste) were painted onto polished surfaces of the sintered ceramic discs. The prepared pellets were heated to 850 °C for 1 h and then slowly cooled to RT. For the electric characterisation of most of the samples, a 10 K step was chosen in the 90–480 K range, and the temperature was controlled using a Cryostat Janis VPF700 coupled to a Lake Shore 331 temperature controller. In the case of samples with low conductivity ($x \geq 0.25$), the electrical characterisation was extended to 800 K using a home-made jig with a controlled N_2 atmosphere. The electric behaviour of the materials was studied using an automatically controlled Agilent Precision LCR E4980-A apparatus in the frequency range of 20–2 MHz. All the measurements were performed under vacuum or inert atmosphere. The impedance data analysis was performed using the “derivative criterion” [18] and non-linear least-square fittings were obtained with the ZView2 programme.

3. Results

3.1. X-ray diffraction

Fig. 2 shows the powder X-ray diffraction (XRD) patterns recorded at room temperature of samples $La_{1/2-x}Li_{1/2-x}Sr_{2x}TiO_3$ with $x = 0.0312$, 0.125, 0.25 and 0.375. All of the samples exhibited typical ABO_3 perovskite diffraction peaks that were indexed on a primitive cubic perovskite cell ($a_p \times a_p \times a_p$). As the Sr content was increased, the XRD peaks shifted to lower angles, which indicates that lattice parameters increase with Sr content, in agreement with the larger ionic radii of Sr^{2+} (1.44 Å) compared to that of La^{3+} (1.32 Å). In the case of the sample with the lowest x value ($x = 0.0312$), broad peaks (labelled with asterisks) associated with a doubled tetragonal perovskite were detected. Additional small peaks (labelled with arrows) associated with a Li_2TiO_3 impurity were also detected; however, the peak intensity of this impurity was estimated to be less than 1%.

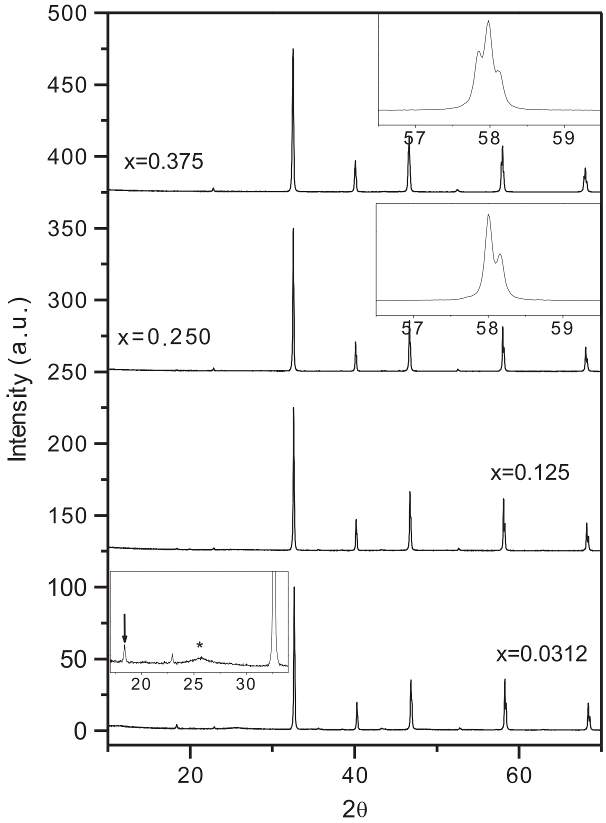

Fig. 2. Powder X-ray diffraction patterns of $La_{1/2-x}Li_{1/2-x}Sr_{2x}TiO_3$ perovskites with compositions $x=0.0312$, 0.125, 0.250 and 0.375. For the samples with the lowest Sr composition, the magnified version of the low 2θ range of the pattern indicates the presence of small amounts of Li_2TiO_3 (indicated by the arrow). The amorphous halo around the superstructure peaks of a double perovskite (labelled with an asterisk) suggests the presence of extended defects associated to some cation ordering [15].

In the case of samples with the largest amount of Sr ($x\geq0.375$), additional peaks were detected at 2θ values lower than those of the main perovskite peaks (see the upper inset of Fig. 2). These peaks correspond to a Sr-rich perovskite with larger unit-cell parameters, which indicates that some segregation occurs in these compositions. The presence of this phase was used here to define the Sr solubility in the $La_{1/2-x}Li_{1/2-x}Sr_{2x}TiO_3$ solid solution.

3.2. Microstructural characterisation of sintered samples

SEM micrographs of the sintered samples are depicted in Fig. 3. A combination of BSE and EDS detectors were used to analyse the homogeneity of samples and to identify possible secondary phases.

The microstructures of the samples with compositions that range from $x=0.0625$ to 0.25 correspond to homogeneous and well-densified samples. This microstructure corresponds to the nominal perovskites detected by XRD and EDS (Table 1). Few pores (black contrast in the micrographs) are observed in samples in this compositional range. This porosity is especially important in samples with the highest Sr content ($x\geq0.312$).

The micrograph of the sample with $x=0.0312$ shows the presence of a small amount of a secondary phase that appears as areas of dark-grey contrast in the BSE images. EDS analyses of this impurity showed the absence of Sr and La (sample labelled as II in Table 2), which indicates an elemental composition consistent with either a titanium oxide or a lithium titanate. In the case of the major light-grey-contrast phase, the composition obtained by EDS analysis is in good agreement with the nominal composition of the sample.

The sintering of the samples with $x=0.375$ is clearly worse than that achieved with the other compositions, and numerous cracks appear in the compact, as shown in the SEM images. In these samples, two different grain morphologies with different compositions are distinguished. EDS analysis indicated that La is almost absent in the agglomerated particles (labelled as II in Table 2) and that the Sr/Ti ratios approach 1; these results suggest that this phase is $SrTiO_3$.

3.3. Electrical conductivity

Fig. 4a shows room-temperature impedance diagrams for samples with $x=0.0625$ and 0.125. The main semicircle shown in the figure corresponds to the grain-boundary contribution (capacitance of approximately 10^{-9}–10^{-10} F). The bulk contribution was detected at high frequencies; however, the full semicircle could not be displayed except in the case of the $La_{0.375}Li_{0.375}Sr_{0.25}TiO_3$ ($x=0.125$) sample. The samples had to be cooled to 210 K (inset of Fig. 4a) to acquire the full semicircle of the other three samples.

The frequency dependence of the real part of the conductivity indicates behaviour typical of fast ionic conductors (Fig. 4b). In Sr-poor samples ($x\leq0.125$), a dc plateau ascribed to the bulk contribution was detected at high frequencies. The decay of the conductivity observed at low frequencies was assigned to ion blocking at the grain boundaries. The conductivity decreased as the Sr content increased; moreover, a displacement of the bulk conductivity plateau to lower frequencies was observed.

For samples with $x\geq0.150$, the characteristic dc conductivity plateau was not detected, which suggests the absence of long-range ionic mobility. The erratic values observed at low frequencies for $x=0.250$ are produced by the high impedance of the samples, which are out of the impedance range of the measurements.

The evolution of the bulk dc ionic conductivity with temperature is shown in Fig. 5. The sample with the lowest Sr content exhibited the best conductivity values. As the Sr content increased, the conductivity decreased, and for samples with $x\geq0.25$, it was diminished considerably; the dc conductivity of these samples could only be measured at higher temperatures.

4. Discussion

In the prepared samples, one Li^+ and one La^{3+} are replaced by two Sr^{2+} in $La_{1/2}Li_{1/2}TiO_3$. The valence of the Ti^{4+} cations does not change, and charge neutrality is preserved along the series. X-ray analyses indicate the apparent formation of a

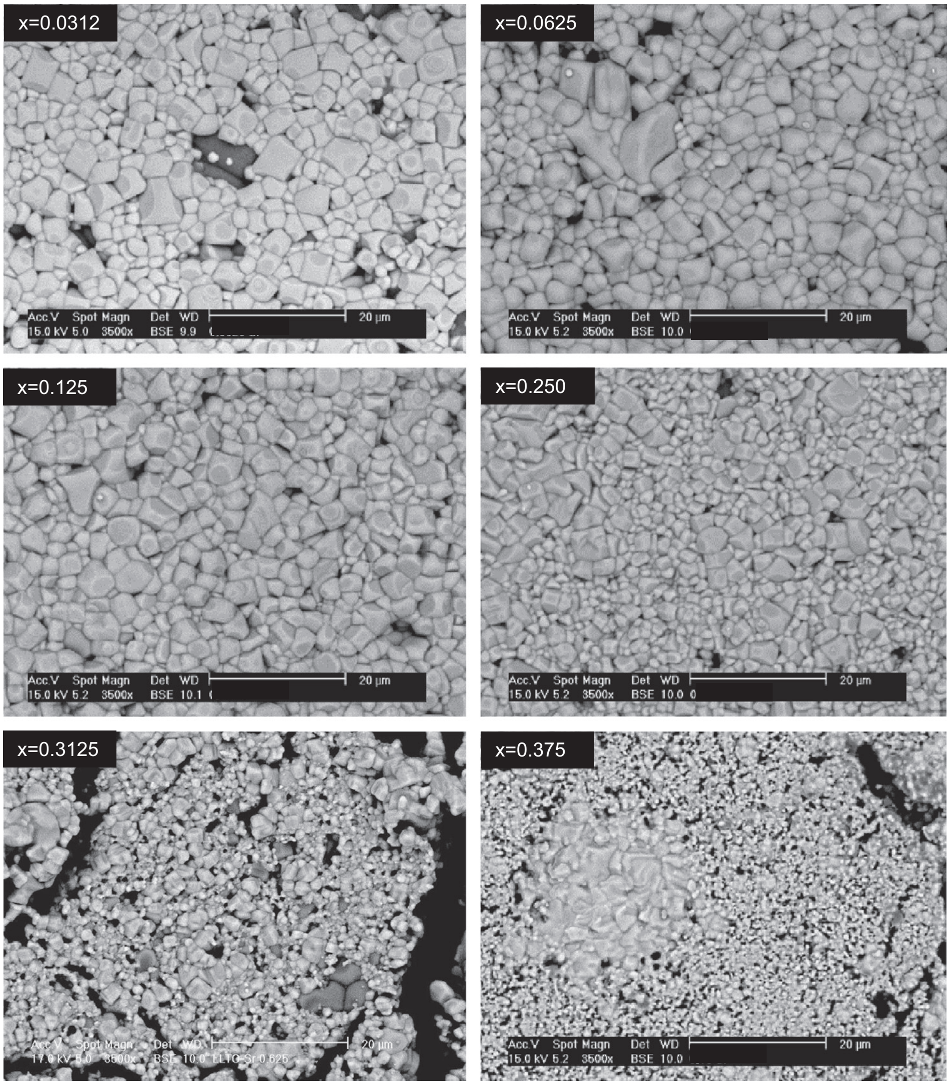

Fig. 3. Scanning electron micrograph obtained with the BSE detector for different compositions of the $Li_{1/2-x}Sr_{2x}La_{1/2-x}TiO_3$ series ($x=0.0312$, 0.0625, 0.125, 0.250 and 0.375).

Table 1

EDS microanalysis results for the single phase or biphasic areas found in $La_{1/2-x}Li_{1/2-x}Sr_{2x}TiO_3$ compositions. The La:Sr:Ti ratio is also indicated for each composition. (I) and (II) denote the main phase (Li-perovskite) and the secondary phase, respectively, in biphasic samples.

x	0.031 (I)	0.031 (II)	0.062	0.125	0.15	0.250	0.3125 (I)	0.3125(II)	0.375 (I)	0.375 (II)
La	**15.4**	0	**14.0**	**11.7**	**11.0**	**7.4**	**6.3**	**2.9**	**6.5**	**1.6**
Sr	**2.4**	0	**4.2**	**8.3**	**10.1**	**15.8**	**18.2**	**25.5**	**18.6**	**26.2**
Ti	**32.0**	**75.4**	**33.1**	**31.6**	**31.9**	**30.9**	**31.3**	**32.0**	**31.0**	**31.3**
O	**50.2**	**24.6**	**48.7**	**48.4**	**47.0**	**48.0**	**44.2**	**39.6**	**43.9**	**40.9**
La:Sr:Ti	**0.48:0.07:1.00**	–	**0.42:0.126:1.00**	**0.37:0.26:1.00**	**0.345:0.317:1.00**	**0.24:0.51:1.00**	**0.20:0.58:1.00**	**0.09:0.80:1.00**	**0.21:0.60:1.00**	**0.05:0.84:1.00**

The results shown are the averaged analysis results for five different crystallites.

homogeneous $La_{1/2-x}Li_{1/2-x}Sr_{2x}TiO_3$ solid solution in the $0.0625 \leq x \leq 0.25$ compositional range.

Vegard's law is a linear empirical approximation that describes the relationship between lattice parameters and the composition of solid solutions. In accordance with ionic radii, lattice parameters of samples should increase linearly with the Sr content, from 3.8763 Å ($x=0.0312$) to 3.8930 Å ($x=0.25$). In Fig. 6, the unit-cell parameter is plotted as a function of the Sr content in the $La_{1/2-x}Li_{1/2-x}Sr_{2x}TiO_3$ series. As illustrated in the figure, the unit-cell parameter follows a smooth curve, showing an upward departure from the linear prediction of Vegard's law (solid line). This positive deviation was also

Table 2
Structural parameters deduced from X-ray powder diffraction data of $La_{1/2-x}Li_{1/2-x}Sr_{2x}TiO_3$ perovskites. All the patterns were refined in the cubic Pm-3m space group (N° 221) (see Ref. [16]).

x	0.0312	0.0625	0.125	0.150	0.165	0.250	0.3125 (I)	0.3125 (II)	0.375 (I)	0.375 (II)
a (Å)	3.8763 (1)	3.8800 (1)	3.8857 (1)	3.8864 (1)	3.8881(1)	3.8930 (1)	3.8950	3.9033	3.8959(1)	3.9044 (1)
$B_{La(Sr)}$ (Å^2)	0.446 (1)	0.482(1)	0.475 (1)	0.468 (2)	0.501 (1)	0.487 (1)	0.565	0.413	0.562	0.403
B_{Ti} (Å^2)	0.612 (2)	0.693 (1)	0.607 (3)	0.727 (4)	0.698 (1)	0.701 (1)	0.728	0.555	0.727	0.547
B_O (Å^2)	1.263 (3)	1.209 (2)	1.210 (4)	1.161 (6)	1.204 (1)	1.149 (1)	0.961	0.944	0.962	0.934
dLa–O (Å)	2.7409	2.7436	2.7476	2.7481	2.7493	2.7528	2.7542	2.7601	2.7548	2.7608
dTi–O (Å)	1.9381	1.9400	1.9429	1.9432	1.9440	1.9465	1.9475	1.9517	1.9479	1.9522
La(occ)	0.490	0.460	0.402	0.351	0.330	0.250	0.213	0.025	0.189	0.002
Sr(occ)	0.049	0.111	0.230	0.300	0.344	0.500	0.597	0.981	0.615	0.988
R_p	8.13	8.11	7.95	6.48	7.39	7.59	7.05	7.05	7.53	7.53
R_{wp}	10.5	10.7	10.4	8.91	10.4	9.96	9.41	9.41	9.89	9.89
χ^2	3.25	3.09	2.95	4.48	2.90	3.40	4.15	4.15	3.41	3.41
R_B	7.28	8.09	5.94	4.49	3.72	3.56	5.24	6.23	5.32	5.47
R_F	6.22	6.39	5.19	3.55	2.23	2.37	3.77	5.35	2.62	3.55
wt%		100	100	100	100	100	77.3	22.7	61.66	38.34

B_i denotes the isotropic thermal factors of the different ions (i subscript); the metal–oxygen distances and the weight phase percentage(wt%) are also calculated; R_p, R_{wp}, χ^2 and R_B are the conventional agreement factors given by the Refinement Programme.

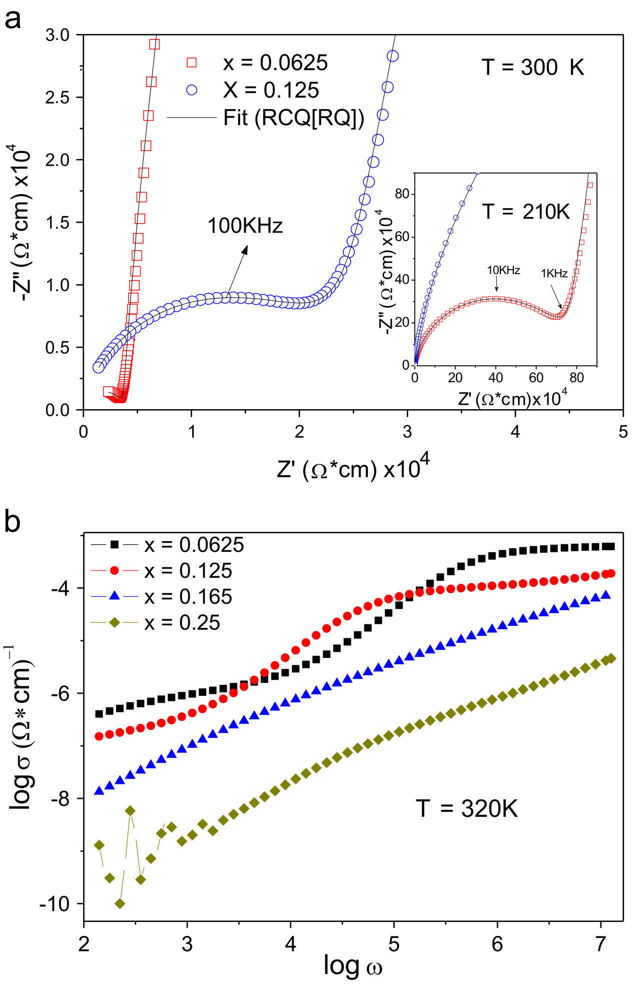

Fig. 4. (a) Complex impedance diagrams of samples with different Sr contents, measured at 300 K and at 210 K (inset). (b) Evolution of the conductivity with the frequency for different compositions in the $La_{1/2-x}Li_{1/2-x}Sr_{2x}TiO_3$ system.

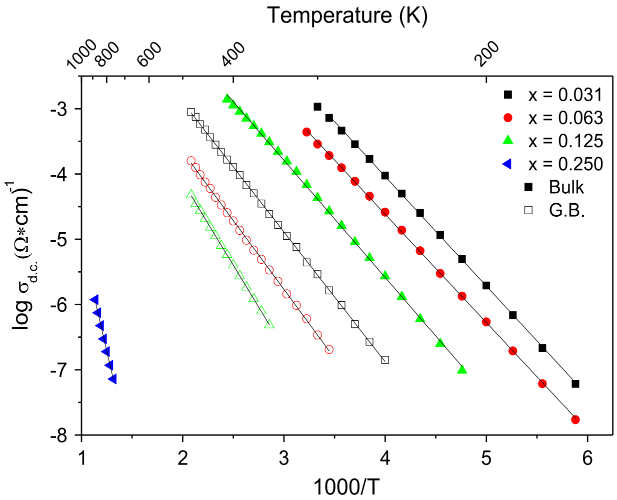

Fig. 5. Temperature dependence of the Li conductivity in $La_{1/2-x}Li_{1/2-x}Sr_{2x}TiO_3$ samples.

observed with respect to the unit-cell volume. A similar trend has been reported for the Li_2TiO_3–MgO solid solution [19], where the deviation was attributed to the presence of some incipient cation clustering in apparently homogeneous samples. A similar deviation has also been described for the SnO_2–TiO_2 system [20–22], where the deviation from Vegard's law was attributed to the minimisation of the elastic strains while the structural coherency of the crystals was maintained [23].

The presence of two-phases in the Sr-rich samples ($x > 0.25$) was detected by XRD and SEM. The analysis of the unit-cell parameters of both phases suggests the segregation of a Sr-rich phase with a composition close to $SrTiO_3$. However, for Sr-poor samples ($x \leq 0.125$), the presence of an amorphous halo at the characteristic peaks of the doubled perovskite ($2\theta \approx 25.6$ and 34.7°) was attributed to the presence of strains and extended stacking faults, which resulted in broadened peaks [15,24,25]. Further studies should be conducted to ascribe the observed deviations from Vegard's law to microstrains associated with extended defects and/or to incipient cation segregation at the nanoscale level. To minimise these effects, other synthesis methods may be required.

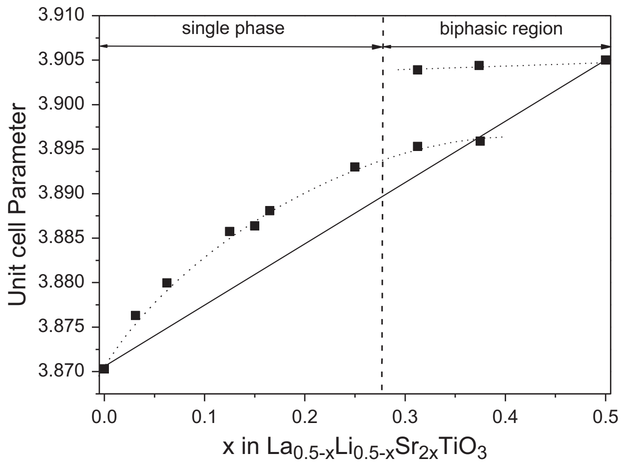

Fig. 6. Plot of the unit-cell lattice parameters as a function of the Li content in $La_{1/2-x}Li_{1/2-x}Sr_{2x}TiO_3$ perovskites. For comparison, values deduced according to Vegard's law are also indicated (solid line).

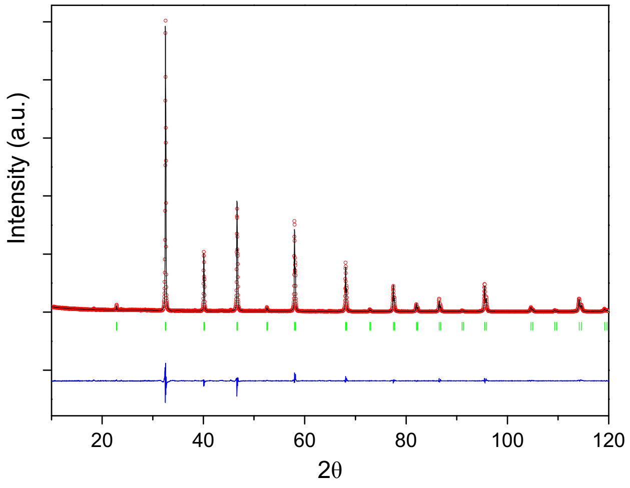

Fig. 7. Observed (open circles), calculated (full line) and difference (bottom) XRD profiles for $La_{0.25}Li_{0.25}Sr_{0.5}TiO_3$. Vertical bars denote Bragg positions.

In particular, the Pechini-type polymerisable precursor method [26] yielded well-crystallised lithium lanthanum titanates (LLTO) at a much lower temperature (900 °C) and with a shorter synthesis time (2 h) compared to those used in the conventional solid-state reaction method. The use of low-temperature synthesis methods may allow samples with a higher homogeneity and an extended solid solution range to be obtained.

In the second stage of our study, we analysed XRD patterns using the Rietveld method. For the end-term of the series (i.e., $La_{0.5}Li_{0.5}TiO_3$), different structural models have been proposed [16]. We first used a double perovskite ($a_p \times a_p \times 2a_p$) with tetragonal symmetry and space group P4/mmm (N° 123); however, the absence of sharp super-structure peaks made the adoption of a higher-symmetry unit cell more convenient. Patterns were successfully refined in the single cubic perovskite ($a_p \times a_p \times a_p$) with space group Pm-3m (N° 221), where La and Sr are randomly distributed on the unique A-site of the perovskite. The structural parameters deduced from Rietveld analysis are given in Table 2. The results in this table include the unit cell, the atomic and isotropic thermal parameters (B) and the agreement factors obtained in the final refinements. During the refinements, the lithium contribution to the XRD patterns was not considered because of its small scattering factor. The La and Sr contents were first constrained to nominal compositions; however, these occupancies were considered for the last refinements. Fig. 7 illustrates the goodness of the fit obtained with the Rietveld analyses. Because of the limitations of the XRD technique, other structural models associated with different octahedral tiltings, such as the rhombohedral model detected by neutron diffraction experiments in the $La_{0.5}Li_{0.5}TiO_3$ composition [27,28], cannot be disregarded.

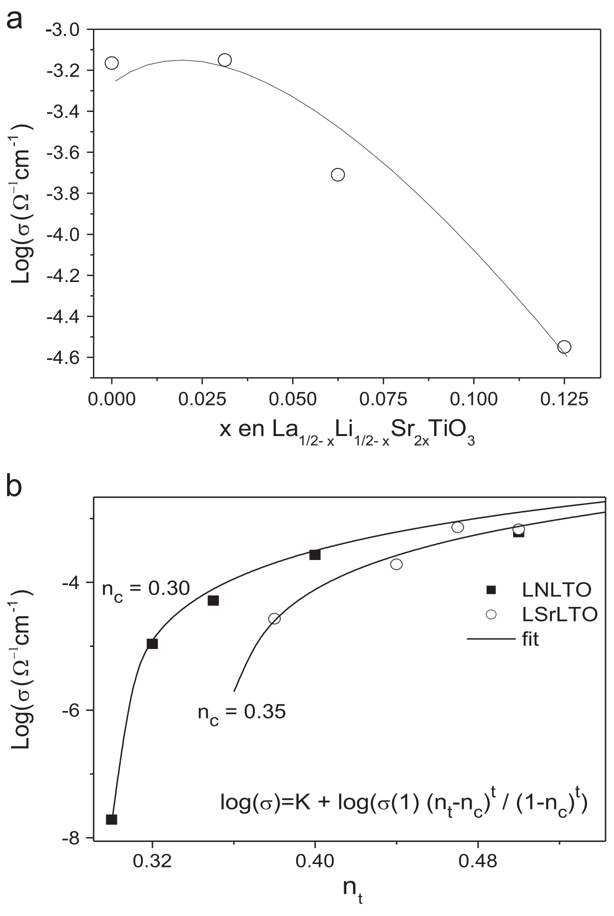

Fig. 8. (a) Bulk ionic conductivity of $La_{1/2-x}Li_{1/2-x}Sr_{2x}TiO_3$ perovskites as a function of the Sr content at room temperature. (b) Conductivity as a function of the effective vacancy concentration (n_t) of two series: $Li_{0.5-x}Na_xLa_{0.5}TiO_3$ (LNLTO) values (black squares) are taken from Ref. [30] and $La_{1/2-x}Li_{1/2-x}Sr_{2x}TiO_3$ (LSrLTO) values (open circles) correspond to the solid solution under investigation. The lines represent fittings to the percolation equation depicted in the plot with $K=-1.84$ and $t=2$.

Dc-conductivity values measured at 300 K in $La_{1/2-x}Li_{1/2-x}Sr_{2x}TiO_3$ samples are plotted as a function of the lithium content in Fig. 8a. The dc conductivity slightly increased in samples with small Sr substitutions and achieved a maximum in samples with lithium contents of approximately 0.47 ($x=0.0312$). These results are in good agreement with those reported by Inaguma et al. [29]; however, in the present work, the compositional range investigated by Inaguma et al. was considerably extended. The slight increase detected in the conductivity of Sr-poor samples has been attributed to the increase in the unit-cell volume, which facilitates lithium diffusion. However, the increase observed in the pre-exponential factors of conductivity, which are associated with the cation vacancy disordering, could also contribute to the observed increase [13,30]. The subsequent decrease in the conductivity of almost two orders of magnitude has been related to the decrease in the concentration of charge carriers and the blockade of A-site vacancies by Sr in the conduction pathways of perovskites. The main differences observed between $La_{2/3-x}Li_xSr_xTiO_3$ ($0.04 \leq x \leq 0.29$) [13] and the $La_{1/2-x}Li_{1/2-x}Sr_{2x}TiO_3$ solid solutions are related to the vacancy concentrations in their perovskite structures. In the former series, the substitution of La by (Sr+Li) decreases the amount of nominal vacancies but maintains the amount of effective vacancies, n_t, that participate in the conduction process. In the solid solution studied in this paper, the nominal vacancy concentration does not change ($\Upsilon=0$) along the series. However, effective vacancies (n_t) are progressively eliminated during Sr incorporation, and the conductivity decreases almost two orders of magnitude near the percolation threshold. The other difference concerns the vacancy ordering, which reduces the dimensionality of the conduction in Sr-poor samples of the former series, whereas, in the solid solution studied here, no La (Sr)-vacancy ordering was observed. The analysis of the conductivity percolation threshold of this series (Fig. 8b) afforded a critical exponent of 2 and a n_c value of 0.35. The percolation threshold was greater than expected for 3D conductivity ($n_c=0.31$), which suggests the existence of some incipient phase segregation. The non-conducting Sr segregated domains will interrupt, in some extent, conduction pathways of the Li-conducting phase, thereby resulting in an increase in the percolation threshold. This effect was not observed in the cubic $Li_{0.5-x}Na_xLa_{0.5}TiO_3$ series [14], where $n_c=0.30$ and where heterogeneities were not detected.

In all cases, the lithium motion was thermally activated, with activation energies of approximately 0.34 ± 0.02 eV for the best conductors and approximately 1.33 ± 0.02 eV for the worst conductors ($x=0.25$) (see Table 3). In the analysed samples, the bulk activation energy does not change linearly with the composition; however, the grain-boundary activation energy varies between 0.39 eV and 0.50 eV as the Sr content increases. Notably, the substantially greater activation energy (1.33 eV) found in the sample with a high Sr content ($x=0.250$) is related to the absence of Li conductivity. In this sample, the effective vacancy concentration, n_t, is below the percolation threshold for the Li conductivity ($n_c=0.35$, see Fig. 8b).

Table 3
Activation energy values calculated from the impedance data for bulk and grain boundary (g.b.) conductivities.

Activation energy		
x	Bulk (eV)	Grain boundary (eV)
0.031	0.33 ± 0.02	0.39 ± 0.02
0.061	0.33 ± 0.02	0.42 ± 0.02
0.125	0.36 ± 0.02	0.51 ± 0.02
0.250	1.33 ± 0.02	

5. Conclusions

The structure and transport properties of samples with compositions along the $Li_{1/2}La_{1/2}TiO_3$–$SrTiO_3$ line of the phase diagram were investigated. A cubic solid solution, $La_{1/2-x}Li_{1/2-x}Sr_{2x}TiO_3$, formed over a relatively wide compositional range of $0.0625 \leq x \leq 0.25$. A biphasic region was observed for Sr-rich samples ($x > 0.25$), where phases close to $SrTiO_3$ were detected.

Samples belonging to the solid solution adopt a single cubic perovskite ($a_p \times a_p \times a_p$) structure, as deduced by XRD experiments. The substitution of Li and La by two Sr ions produced a progressive increase in the unit-cell parameters, which was in agreement with ionic radii of atoms; however, a positive deviation from Vegard's law was observed, which was attributed to deviations from the random distribution of La and Sr cations.

The results described in this work confirm the important role played by effective vacant A-sites, n_t, on the Li conductivity in perovskites. In the $La_{1/2-x}Li_{1/2-x}Sr_{2x}TiO_3$ series, the amount of A-site nominal vacancies, Υ, was not modified; however, the total amount of effective vacant A-sites, given by the expression $n_t=[Li]+\Upsilon$, was progressively reduced. This decrease in effective vacant A-sites substantially diminishes the lithium dc conductivity when n_t approaches the 3D percolation threshold of vacancies in perovskites. In this series, the percolation threshold is larger ($n_c=0.35$) than expected ($n_c=0.30$), which suggests the existence of an incipient cation segregation on the nanometre scale. The activation energy of samples belonging to the solid solution is 0.32 eV, which is similar to the 0.34 eV reported as one of the lowest activation energies for lithium-ion conductors.

Acknowledgements

The authors thank the Regional (CAM) Government (MATERYENER S2009 PPQ-1626), the National Government (MICINN) (MAT2010-19837-CO6), and the European Programme-IRSES (NANOLICOM) for financial support.

References

[1] A.G. Belous, G.N. Novitskaya, S.V. Polyanetskaya, Y.I. Gornikov, Crystal-chemical and electro-physical characteristics of complex oxides $Ln_{2/3-x}M_{3x}TiO_3$, Zhurnal Neorganicheskoi Khimii 32 (1987) 283–286 (in Russian).
[2] Y. Inaguma, L. Chen, M. Itoh, T. Nakamura, T. Uchida, H. Ikuta, M. Wakihara, High ionic conductivity in lithium lanthanum titanate, Solid State Communications 86 (1993) 689–693.
[3] S. Stramare, V. Thangadurai, W. Weppner, Lithium lanthanum titanates:a review, Chemistry of Materials 15 (21) (2003) 3974–3990.

[4] A. Morata-Orrantia, S. Garcia-Martin, M.A. Alario-Franco, Optimization of lithium conductivity in La/Li titanates, Chemistry of Materials 15 (21) (2003) 3991–3995.

[5] H.-T. Chung, J.-G. Kim, H.-G. Kim, Dependence of the lithium ionic conductivity on the B-site ion substitution in $(Li_{0.5}La_{0.5})Ti_{1-x}M_xO_3$ (M=Sn, Zr, Mn, Ge), Solid-State Ionics 107 (1998) 153–160.

[6] A.G. Belous, Synthesis and electrophysical properties of novel lithium ion conducting oxides, Solid-State Ionics 90 (1996) 193–196.

[7] S. García-Martin, J.M. Rojo, H. Tsukamoto, E. Morán, M.A. Alario-Franco, Lithium-ion conductivity in the novel $La_{1/3-x}Li_{3x}NbO_3$ solid solution with perovskite-related structure, Solid-State Ionics 116 (1999) 11–18.

[8] K. Mizumoto, S. Hayashi, Crystal structure and lithium ion conductivity of A-site deficient perovskites $La_{1/3-x}Li_{3x}TaO_3$, Journal of the Ceramic Society of Japan 105 (1997) 713–715.

[9] M. Itoh, Y. Inaguma, W.H. Jung, L. Chen, T. Nakamura, High lithium ion conductivity in the perovskite-type compounds $Ln_{1/2}Li_{1/2}TiO_3$ (Ln=La, Pr, Nd, Sm), Solid-State Ionics 70–71 (1994) 203–207.

[10] H. Kawai, J. Kuwano, Lithium ion conductivity of A-site deficient perovskite solid solution $La_{0.67-x}Li_{3x}TiO_3$, Journal of the Electrochemical Society 141 (7) (1994) L78–79.

[11] A.D. Robertson, S García-Martín, A. Coats, A.R. West, Phase diagrams and crystal chemistry in the Li^+ ion conducting perovskites, $Li_{0.5-3x}RE_{0.5+x}TiO_3$: RE=La, Nd, Journal of Materials Chemistry 5 (9) (1995) 1405–1412.

[12] T. Katsuma, Y. Matsui, Y. Inaguma, M. Itoh,Influence, of site percolation and local distortion on lithium ion conductivity in perovskite-type oxides $La_{0.55}Li_{0.35-x}K_xTiO_3$ and $La_{0.55}Li_{0.35}TiO_3$–KMO_3 (M=Nb and Ta), Solid-State Ionics 86–88 (1996) 165–169.

[13] W. Bucheli, T. Duran, R. Jimenez, J. Sanz, A. Varez, On the influence of the vacancy distribution on the structure and ionic conductivity of A-site-deficient $Li_xSr_xLa_{2/3-x}TiO_3$ perovskites, Inorganic Chemistry 51 (10) (2012) 5831–5838.

[14] A. Rivera, C. León, J. Santamaría, A. Várez, O. V'yunov, A.G. Belous, J.A. Alonso, J. Sanz, Percolation-limited ionic diffusion in $Li_{0.5-x}Na_xLa_{0.5}TiO_3$ perovskites ($0\leq x\leq 0.5$), Chemistry of Materials 14 (2002) 5148–5152.

[15] A. Varez, F. Garcia-Alvarado, E. Morán, M.A. Alario-Franco, Microstructural study of $La_{0.5}Li_{0.5}TiO_3$, Journal of Solid State Chemistry 118 (1995) 78–83.

[16] J. Ibarra, A. Varez, C. León, J. Santamaría, L.M. Torres-Martínez, J. Sanz, Influence of composition on the structure and conductivity of the fast ionic conductors $La_{2/3-x}Li_{3x}TiO_3$ ($0.03\leq x\leq 0.167$), Solid-State Ionics 134 (2000) 219–228.

[17] J. Rodríguez-Carvajal, Recent advances in magnetic structure determination by neutron powder diffraction, Physica B 192 (1993) 55–69 (Fullprof Program: Rietveld Pattern Matching Analysis of Powder Patterns, Grenoble, ILL, (1990)).

[18] W. Bucheli, R. Jimenez, J. Sanz, A. Varez, The $\log(\sigma)$ vs. $\log(\omega)$ derivative plot used to analyse the ac conductivity. Application to fast Li^+ ion conductors with perovskite structure, Solid State Ionics 227 (2012) 113–118.

[19] M. Castellanos, A.R. West, Deviations from Vegard's law in oxide solid solutions. The systems Li_2TiO_3–MgO and Li_2TiO_3–Na_2TiO_3, Journal of the Chemical Society, Faraday Transactions I 76 (1980) 2159–2169.

[20] T. Hirata, K. Ishioka, M. Kitajima, H. Doi, Concentration dependence of optical phonons in the TiO_2–SnO_2 system, Physical Review B 53 (1996) 8442–8448.

[21] P. Ifeacho, H. Wiggers, P. Roth, SnO_2/TiO_2 mixed oxide particles synthesized in doped premixed H_2/O_2/Ar flames, Proceedings of the Combustion Institute 30 (2005) 2577–2584.

[22] A. Tricoli, M. Righettoni, S.E. Pratsinis, Minimal cross-sensitivity to humidity during ethanol detection by SnO_2–TiO_2 solid solutions, Nanotechnology 20 (2009) 315502.

[23] F.R. Sensato, R. Custodio, E. Longo, A. Beltran, J. Andres, Electronic and structural properties of $Sn_xTi_{1-x}O_2$ solid solutions: a periodic DFT study, Catalysis Today 85 (2003) 145–152.

[24] S. Garcia-Martin, M.A. Alario-Franco, H. Ehrenberg, J. Rodriguez-Carvajal, U. Amador, Crystal structure and microstructure of some $La_{2/3-x}Li_{3x}TiO_3$ oxides: an example of the complementary use of electron diffraction and microscopy and synchrotron X-ray diffraction to study complex materials, Journal of the American Chemical Society 126 (11) (2004) 3587–3596.

[25] J.L. Fourquet, H. Duroy, M.P. Crosnier-Lopez, Structural and microstructural studies of the series $La_{2/3-x}Li_{3x}TiO_3$, Journal of Solid State Chemistry 127 (1996) 283–294.

[26] M. Vijayakumar, Y. Inaguma, W. Mashiko, M.P. Crosnier-Lopez, C. Bohnke, Synthesis of fine powders of $Li_{3x}La_{2/3-x}TiO_3$ perovskite by a polymerizable precursor method, Chemistry of Materials 16 (2004) 2719–2724.

[27] J.A. Alonso, J. Sanz, J. Santamaria, C. Leon, A. Varez, M.T. Fernandez-Diaz, On the location of Li^+ cations in the fast Li-cation conductor $La_{0.5}Li_{0.5}TiO_3$ perovskite, Angewandte Chemie International Edition 3 (2000) 619.

[28] A Varez, M.T. Fernandez-Diaz, J.A. Alonso, J. Sanz, Structure of fast ion conductors $Li_{3x}La_{2/3-x}TiO_3$ deduced from powder neutron diffraction experiments, Chemistry of Materials 17 (2005) 2404–2412.

[29] Y. Inaguma, L. Chen, M. Itoh, T. Nakamura, Candidate compounds with perovskite structure for high lithium ionic conductivity, Solid State Ionics 70–71 (1994) 196–202.

[30] R. Jimenez, A. Varez, J. Sanz, Influence of octahedral tilting and composition on electrical properties of the $Li_{0.2-x}Na_xLa_{0.6}TiO_3$ ($0\leq x\leq 0.2$) series, Solid State Ionics 179 (2008) 495–502.